The role of ETG modes in JET–ILW pedestals with varying levels of power and fuelling

OPEN ACCESS
IOP Publishing | International Atomic Energy Agency Nuclear Fusion

Nucl. Fusion **62** (2022) 086028 (16pp) https://doi.org/10.1088/1741-4326/ac7476

The role of ETG modes in JET–ILW pedestals with varying levels of power and fuelling

B. Chapman-Oplopoiou[1,*], D.R. Hatch[2], A.R. Field[1], L. Frassinetti[3], J.C. Hillesheim[1], L. Horvath[1], C.F. Maggi[1], J.F. Parisi[1,4], C.M. Roach[1], S. Saarelma[1], J. Walker[2] and JET Contributors[a]

[1] UKAEA-CCFE, Culham Science Centre, Abingdon, OX14 3DB, United Kingdom
[2] Institute for Fusion Studies, University of Texas at Austin, Austin, TX 78712, United States of America
[3] Division of Fusion Plasma Physics, KTH, Stockholm, Sweden
[4] Princeton Plasma Physics Laboratory, Princeton University, Princeton, NJ 08543, United States of America

E-mail: benjamin.chapman@ukaea.uk

Received 13 January 2022, revised 12 May 2022
Accepted for publication 30 May 2022
Published 22 June 2022

Abstract

We present the results of GENE gyrokinetic calculations based on a series of JET–ITER-like-wall (ILW) type I ELMy H-mode discharges operating with similar experimental inputs but at different levels of power and gas fuelling. We show that turbulence due to electron-temperature-gradient (ETGs) modes produces a significant amount of heat flux in four JET–ILW discharges, and, when combined with neoclassical simulations, is able to reproduce the experimental heat flux for the two low gas pulses. The simulations plausibly reproduce the high-gas heat fluxes as well, although power balance analysis is complicated by short ELM cycles. By independently varying the normalised temperature gradients (ω_{T_e}) and normalised density gradients (ω_{n_e}) around their experimental values, we demonstrate that it is the ratio of these two quantities $\eta_e = \omega_{T_e}/\omega_{n_e}$ that determines the location of the peak in the ETG growth rate and heat flux spectra. The heat flux increases rapidly as η_e increases above the experimental point, suggesting that ETGs limit the temperature gradient in these pulses. When quantities are normalised using the minor radius, only increases in ω_{T_e} produce appreciable increases in the ETG growth rates, as well as the largest increases in turbulent heat flux which follow scalings similar to that of critical balance theory. However, when the heat flux is normalised to the electron gyro-Bohm heat flux using the temperature gradient scale length L_{T_e}, it follows a linear trend in correspondence with previous work by different authors.

Keywords: tokamak, pedestal, gyrokinetics, turbulence, ETG, JET, ITER

(Some figures may appear in colour only in the online journal)

* Author to whom any correspondence should be addressed.
[a] See the author list of J. Mailloux *et al* to be published in Nuclear Fusion Special issue: Overview and Summary Papers from the 28th Fusion Energy Conference (Nice, France, 10-15 May 2021).

1. Introduction

The transition to high confinement, H-mode [1], is considered an essential ingredient to the successful operation of most future tokamaks such as ITER. The H-mode transition occurs when a threshold in input heating power is crossed and the turbulent transport is strongly suppressed at the edge—an edge transport barrier. The steep gradient region of this transport barrier is known as the pedestal, which has significantly higher edge densities and temperatures that propagate into the core, improving confinement. However, turbulent transport is not entirely suppressed within the pedestal, and the steep density and temperature gradients provide a significant source of free energy for microinstabilites, which manifest as plasma turbulence in their saturated nonlinear state.

The transition of JET from a carbon wall to an ITER-like-wall (ILW) consisting of a tungsten divertor and a beryllium first wall has led to several interesting and complex observations [2–11]. Notably, increased molecular deuterium (D_2) gas puffing is needed to prevent tungsten contamination in the core. This drastically degrades the pedestal top temperature $T_{\mathrm{e,ped}}$, a key measure of plasma performance. Increased input power is therefore needed to sustain robust temperature pedestals. Recent work has highlighted the importance of microinstabilities such as electron temperature gradient modes (ETGs) both the slab and toroidal variants, ITGs (the ion equivalents of ETG modes), kinetic-ballooning-modes (KBM) and micro-tearing-modes (MTM) in the pedestal region of tokamak plasmas [12–24]. In reference [14], it was shown that a combination of neoclassical, ETG, ITG, and MTM transport is in good agreement with measurements of the power crossing the separatrix (P_{sep}) in selected JET–ILW and JET–C plasmas. In particular, ETG transport was found to provide the dominant contribution to JET–ILW heat transport. The parameter that determines the instability threshold for the slab-branch of ETG modes is the ratio between the normalised temperature and density gradients $\eta_{\mathrm{e}} = \omega_{T_{\mathrm{e}}}/\omega_{n_{\mathrm{e}}}$ (where $\omega_{T_{\mathrm{e}}} = -\nabla T_{\mathrm{e}}/T_{\mathrm{e}} = 1/L_{T_{\mathrm{e}}}$ and $\omega_{n_{\mathrm{e}}} = -\nabla n_{\mathrm{e}}/n_{\mathrm{e}} = 1/L_{n_{\mathrm{e}}}$). This parameter is sensitive to changes in $\omega_{n_{\mathrm{e}}}$, and can quickly become large as $\omega_{n_{\mathrm{e}}}$ becomes small. This is of particular importance for JET–ILW as the increased gas puffing necessary to prevent tungsten accumulation often results in a radially outward shift of the density profile with respect to the temperature profile, which results in a shallow density gradient and therefore a large η_{e} in the pedestal region [9, 25], which is shown to correlate with degraded pedestal pressure. Similarly, increased input power tends to steepen the temperature gradient, raising η_{e} in turn. It is therefore vital to obtain a deeper understanding of how ETG turbulent transport is influenced by gas fuelling and input power. Additionally, it is important top understand how ETG turbulent transport varies with driving parameters such as η_{e}, $\omega_{n_{\mathrm{e}}}$, and $\omega_{T_{\mathrm{e}}}$ which can be heavily influenced by the conditions at the separatrix and are negatively correlated with the total pedestal pressure [25].

To this end, we apply the GENE gyrokinetic code [26, 27] to a JET–ILW experimental dataset [7] comprising four type I ELMy H-mode discharges from scans in the neutral-beam-injected (NBI) power (P_{NBI}) at two levels of D_2 gas fuelling rate ϕ_{e}. All pulses have a low triangularity plasma shape, plasma current $I_{\mathrm{p}} = 1.4$ MA, toroidal magnetic field $B_{\mathrm{T}} = 1.7$ T, and have been well characterised experimentally [6, 7, 9, 28]. To aid our discussion, we introduce the following nomenclature: 'L' and 'H' refer to 'low' and 'high' respectively; whereas 'P' and 'G' refer to 'power' and 'gas' respectively. For example, HPHG refers to a pulse with high power and high gas, LPHG refers to a pulse with low power and high gas, and so on. The low and high power pulses have $P_{\mathrm{NBI}} \simeq 4.5$ MW and $\simeq 15$ MW respectively. The pulses at low and high gas rate have $\phi_{\mathrm{e}} \simeq 2.7 \times 10^{21}$ es^{-1} and $\simeq 18.0 \times 10^{21}$ es^{-1} respectively. In figure 1 we plot four density n_{e} and electron temperature T_{e} profiles from our dataset as a function of flux surface (radial) coordinate ρ_t. The profiles are obtained by Thomson scattering (TS) measurements which are subsequently fitted with a modified tanh (mtanh) function in the pre-ELM (80%–99%) time interval [29]. The radial positions of the TS profiles are calibrated to match the well justified expectation that $T_{\mathrm{e}} = 100$ eV at the JET–ILW separatrix ($\rho_t = 1$) [30]. The high gas pulses are observed to have a large relative shift between the density and temperature pedestals, the former being shifted radially outwards leading to a much larger separatrix density $n_{\mathrm{e,sep}}$ and lower $\omega_{n_{\mathrm{e}}}$ inside the separatrix region. Profiles of: η_{e}, $\omega_{n_{\mathrm{e}}}$, and $\omega_{T_{\mathrm{e}}}$ are displayed in the top row of figure 2, in which, for a given power, the lower values $\omega_{n_{\mathrm{e}}}$ in the high gas (solid lines) pulses and resulting larger values of η_{e} are apparent. The bottom row of figure 2 plots, from left to right, the safety factor q, normalised magnetic shear $\hat{s} = \left(\rho_t/q\right)\left(\mathrm{d}q/\mathrm{d}\rho_t\right)$, and the equilibrium flow shear $\gamma_{E\times B}$ profiles. Flow shear is used in the global simulations presented in section 2 and nonlinear simulations presented in sections 3 and 4, and has been estimated from a neoclassical formula [31] by setting the parallel flow $V_{\parallel}$ to zero, an assumption which is often experimentally justified in tokamaks [32]. Irrespective of the validity of this assumption for these pulses, the values of equilibrium flow shear used throughout the simulations presented here can reasonably be assumed to lie well within the large error bars associated with the challenging measurement of this quantity experimentally. Indeed, our flow shear calculations predict that the high gas pulses have lower equilibrium flow shear than their low gas counterparts, which is expected and can be understood in terms of the neoclassical force balance—the reduced $\omega_{n_{\mathrm{e}}}$ inside the separatrix reduces the ion pressure gradient and therefore the equilibrium flow shear.

The paper is organised as follows. To introduce the four pulses and motivate our focus on ETG modes, section 2 briefly examines the range of micro-instabilities present across the pedestal region. Section 3 contains a key result of this paper and comprises nonlinear simulations of ETG turbulence, which are discussed in the context of experimental measurements. Linear and nonlinear scans of $\omega_{T_{\mathrm{e}}}$ and $\omega_{n_{\mathrm{e}}}$ are presented in section 4 in an effort to understand the linear driving mechanisms behind the ETG modes reported here as well as how the turbulent heat transport changes in response to profile changes.

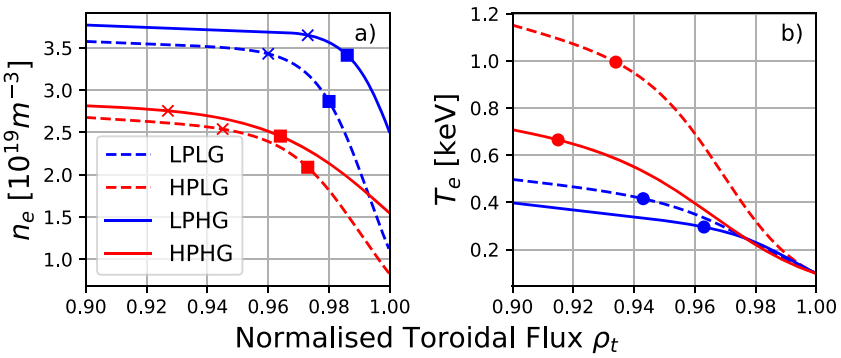

Figure 1. TS n_e (a) and T_e (b) profiles used in some of the GENE simulations throughout. Blue (red) lines denote low (high) power pulses, and dashed (solid) lines denote low (high) gas pulses. Circles, crosses, and squares denote the locations of flux surfaces **A**, **B**, and **C** respectively, see main text.

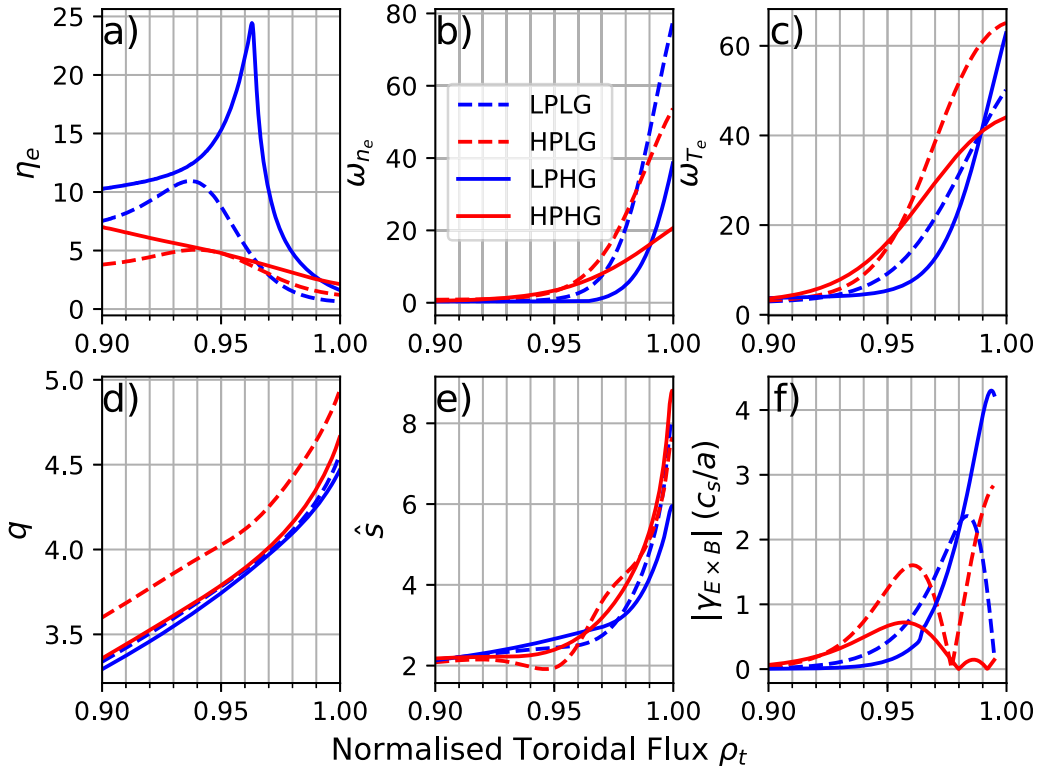

Figure 2. Blue (red) lines denote low (high) power pulses, and dashed (solid) lines denote low (high) gas pulses. All traces are plotted as a function of magnetic co-ordinate ρ_t (a) $\eta_e = \omega_{T_e}/\omega_{n_e}$, ($b$) normalised temperature gradient $\omega_{T_e} = 1/L_{T_e}$, (c) normalised density gradient $\omega_{n_e} = 1/L_{n_e}$, (d) q-profile, (e) normalised magnetic shear $\hat{s}$, (f) magnitude of equilibrium flow shear estimate using neoclassical force balance.

We summarise our results in section 5 and propose avenues of future enquiry.

2. An overview of the micro-instabilities in these pulses

Throughout this manuscript, we endeavour to retain as many physical effects as possible in our GENE simulations. All simulations are electromagnetic, collisional, and include full toroidal effects. The numerical equilibria are calculated self-consistently with the pre-ELM TS profiles shown in figure 2 using the HELENA code [33]. For the pulses investigated in this manuscript, there were no accurate measurements of the ion temperature profile in the steep gradient region of the pedestal. As a bounding assumption we set the ion temperature profile equal to the electron temperature profile throughout this work. This assumption is valid in the pedestal top region, where it is often the case that $T_{\mathrm{i,ped}} = T_{\mathrm{e,ped}}$. At the separatrix, we expect $T_{\mathrm{i,sep}} \geqslant T_{\mathrm{e,sep}}$ [28]. These two bounds lead us to $\omega_{T_\mathrm{i}} \leqslant \omega_{T_\mathrm{e}}$ throughout the steep gradient region. Therefore, our simulations, which set $\omega_{T_\mathrm{i}} = \omega_{T_\mathrm{e}}$ may overestimate ITG and KBM growth rates in some cases. Conversely, $\omega_{T_\mathrm{i}} < \omega_{T_\mathrm{e}}$ would decrease the equilibrium flow shear rate $\gamma_{E\times B}$ which is proportional to the ion pressure gradient, meaning

the assumption $\omega_{T_\mathrm{i}} = \omega_{T_\mathrm{e}}$ may underestimate ITG and KBM growth rates in some cases (although, the dominant contributor to $\gamma_{E\times B}$ is the density gradient) [14]. In addition, there is a small error in our flow-shear estimation due to the assumption $V_\parallel = 0$. This error was estimated to be in the range 0%–15% in [14]. Therefore, in the context of ITG and KBM modes, our assumption $\omega_{T_\mathrm{i}} = \omega_{T_\mathrm{e}}$ may lead to two competing effects: an overestimate of the drive, and an underestimate of the flow shear damping. Given the emphasis on ETG driven modes in this manuscript, we do not expect this limiting assumption to impact our conclusions qualitatively.

We used the Hager bootstrap current formula for the equilibrium calculation [34] which under predicts the bootstrap current somewhat compared to NEO [35, 36] in our high power pulses, but is in good agreement with NEO for the low power pulses [37]. Results from a large database of pedestal ETG simulations [38] (which includes many of the simulations in the present manuscript), show no discernible correlation between the pedestal ETG turbulent heat flux and the magnetic shear $\hat{s}$. Therefore, we do not expect the uncertainty in the bootstrap current to impact our work significantly. Future studies could try using recently developed Redl [39] bootstrap current formula in the equilibrium reconstruction, as well as assessing the role of $\hat{s}$ on pedestal ETG modes. All simulations model electrons and deuterium kinetically, and all simulations presented in sections 2 and 3 also model a third impurity species which is assumed to be dominated by beryllium. The contribution of beryllium is included in the equilibrium self-consistently using the best available estimates of the effective charge Z_eff as measured by visible Bremsstrahlung radiation. The nonlinear parameter scans presented in section 4 model electrons and deuterium only due to their large computational expense.

We begin by discussing the micro-instabilities present across the pedestals of the four pulses, the resolution parameters for these local simulations can be found in appendix A. Figure 3 shows the results of a series of local-linear simulations for each pulse over a wide range of normalised poloidal wavenumbers $k_y\rho_s$ covering instabilities from KBMs and MTMs ($k_y\rho_s \sim 10^{-1}$), ITG ($k_y\rho_s \sim 1$), and ETG ($k_y\rho_s \gtrsim 1$). To distinguish between different types of modes, we check: the eigenfunction of the mode along the parallel direction, the frequency of the mode and its rotation direction, and the transport fingerprints of the mode [18]. For each k_y, we carried out a seven-point scan in θ_0 (related to the central wavenumber in the x-direction of the simulation domain via $\theta_0 = k_{x,\mathrm{centre}}/\hat{s}k_y$) from $-\pi$ to π passing through $\theta_0 = 0$. This is necessary to properly quantify the existence of pedestal toroidal-ETGs (TETGs), whose growth rate peaks at $\theta_0 \neq 0$ [20, 40]. Additionally, MTMs have also been found to peak at $\theta_0 \neq 0$ in some JET–ILW pedestals [12]. For each k_y and ρ_t, the growth rate displayed in figure 3 is the maximum growth rate over all θ_0. A plot showing an example of how the growth rate of ETG modes varies with both k_y and θ_0 for the HPLG pulse can be seen in figure 4. The modes at $k_y\rho_s \gtrsim 30$ that peak at $\theta_0 = 0$ are primarily sETGs, whereas the modes at $k_y\rho_s \lesssim 30$ that peak away from $\theta_0 = 0$ are a mixture of sETGs and TETGs. Similar plots and a more in-depth discussion of pedestal TETG modes can be found in reference [20].

In figure 3, in general, we see that radially inward of the approximate location of the density pedestal top $\rho_{t,n_\mathrm{e,\,ped}}$ (vertical black-dashed line), for a given value of $k_y\rho_s$, there is little variation in the growth rate of the instability with flux surface. The dominant modes here are ITG/TEM at low $k_y\rho_s$, and 'core-like' ETG (peaked at the outboard midplane) at high $k_y\rho_s$. The only exception to this is an MTM in the LPLG pulse which sits at the top of the temperature pedestal $\rho_{t,T_\mathrm{e,\,ped}}$ at $k_y\rho_s = 0.15$ and peaks at finite θ_0. Radially outward of $\rho_{t,n_\mathrm{e,\,ped}}$, in the steep gradient region, there are ETGs with high growth rates that increasingly dominate as we move outward towards the separatrix, becoming part of the TEM/ETG continuum at $k_y\rho_s \sim 0.5$. The tendency for ETGs to exist at smaller $k_y\rho_s$ in the steep gradient region is particularly noticeable for the high power pulses. This is due to these pulses having a higher normalised temperature gradient than their low power counterparts (see figure 2), which shifts the growth rate spectrum to lower $k_y\rho_s$, as predicted by critical balance theory [41, 42]. At $k_y\rho_s \lesssim 5$, the dominant form of ETG in the steep-gradient region is often the pedestal TETG (distinct in nature from its more traditional counterpart found in the core in that it owes its existence to large values of ω_{T_e} and mostly peaks at $\theta_0 \neq 0$), whereas at higher $k_y\rho_s$, the dominant ETG in this region is the slab mode. The low gas pulses have a KBM enclave in the bottom right corner at $k_y\rho_s \lesssim 0.2$, close to the separatrix (distinguished by its vanishing parallel electric field and transport fingerprints [12, 18]). One can speculate that in the high gas cases, the KBMs have been shifted radially outwards inside the scrape-off-layer (SOL) as the density profile has shifted. However, dealing with KBMs in the pedestal so close to the separatrix is highly problematic. First, the radial extent of these modes often exceeds the width of the pedestal [14], secondly, they exist only for an extremely narrow range of θ_0 close to zero, meaning they are highly susceptible to equilibrium flow shear, an effect that is not included in our local-linear simulations.

To this end, we use GENE in its global mode of operation to compute the growth rates of modes with $k_y\rho_s = 0.05$, 0.1, 0.2, and 0.3 across the four pulses. By using the global version of GENE, we allow the temperature and density profiles to vary across the width of the simulation box, which is important to be included when computing the linear properties of a radially extended mode. Our simulation box spans $\rho_t = 0.94$ to 0.995, and Dirichlet (constant value) boundary conditions are enforced at the radial boundaries with a transition region on each side of the boundary (10% of the radial domain on the inner flux surfaces and 15% close to the separatrix). In these transition regions, Krook damping smoothly ramps up to set fluctuations to zero at the boundary [27]. The rest of the simulation parameters can be found in appendix A.

The results of this calculation are shown in figure 5, both with equilibrium flow shear (unlike the local simulations displayed hitherto) and without flow shear. No KBMs were found in these global calculations, irrespective of equilibrium flow shear. It is possible that KBMs and other MHD-like modes

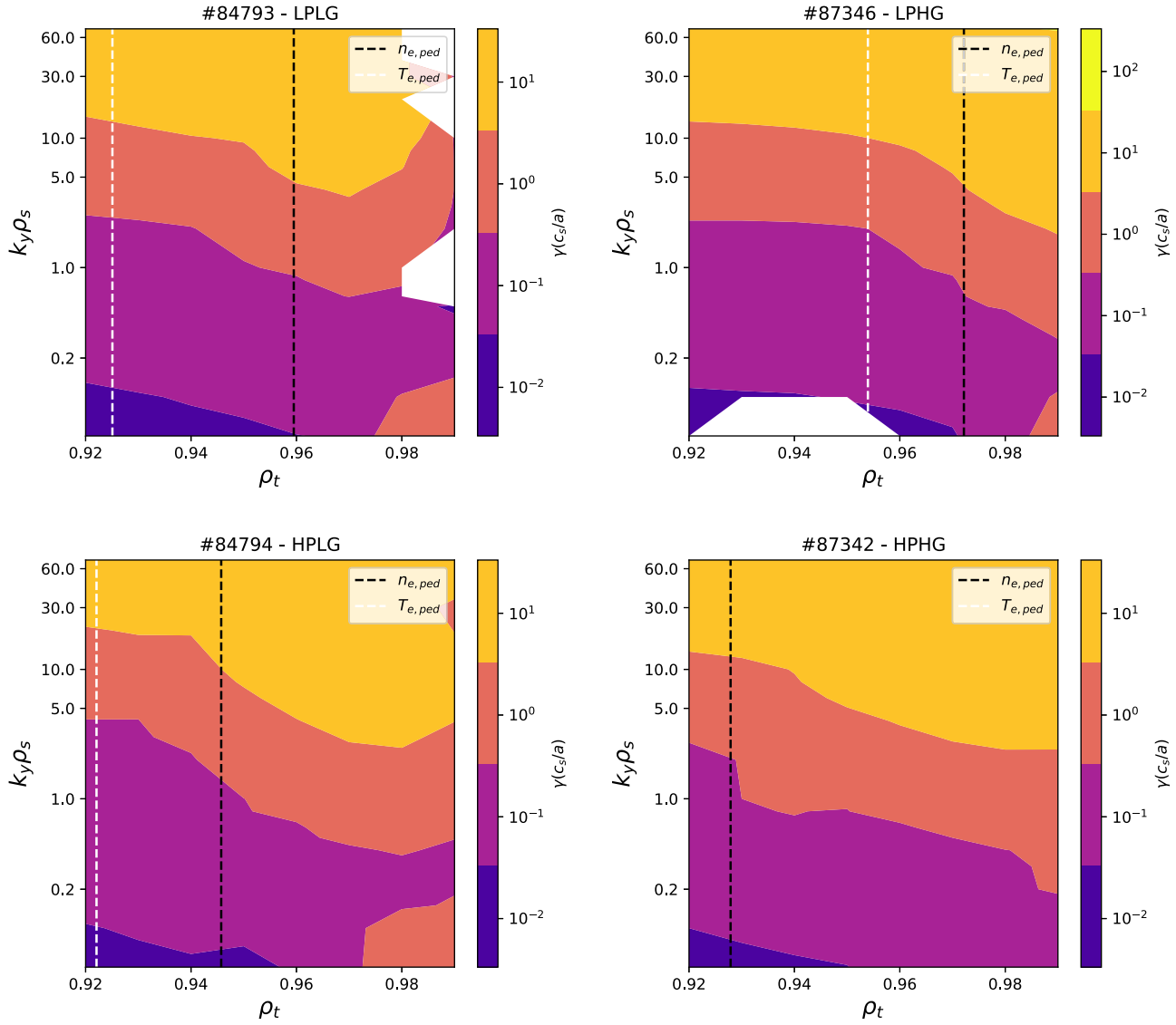

Figure 3. Diagrams giving an overview of the micro-instabilities present in our four pulses. The top row corresponds to low power pulses, the bottom row to high power pulses, the left column to low gas pulses, and the right column to high gas pulses. Each panel displays the growth rate on a $\log_{10}$ scale as a function of the poloidal wavenumber $k_y\rho_s$ and simulated flux surface ρ_t. Vertical lines correspond to the approximate locations of the density (black) and temperature (white) pedestal top (note that in the HPHG pulse the approximate position of the temperature pedestal top is outside of the range of data displayed).

were curtailed by the aforementioned (and restrictive) boundary conditions or the lack of the kink drive term. A coupled pedestal-SOL code, with electromagnetic effects, the inclusion of the kink drive term, as well as $B_\parallel$ fluctuations [43, 44], may be needed to accurately model KBMs in as challenging a regime as JET–ILW pedestals. Codes targetting some of these capabilities (not simultaneously) are under development, but currently not available for routine application to the pedestal [45–48]. The modes shown in figure 5 are ITG/TEM modes, which are mostly sheared away in the low power cases, but survive in the high power cases. This is due to a combination of higher $\omega_{T_i} = \omega_{T_e}$ in the high power cases, and lower γ_E values across the domain of the simulation. A more rigorous analysis of ITG/TEM modes would require details of the ion temperature profiles that are not included in our analysis.

3. Comparison of ETG and neoclassical heat flux with experiment

Having demonstrated the prevalence of ETG modes across the entire pedestal region in figure 3, and confirmed using global GENE simulations that non-local and flow shear affects drastically reduce and even quench the ion scale modes (figure 5), we now turn our attention to the primary focus of this manuscript: the impact of ETG modes on heat transport in the JET–ILW plasmas shown in figure 1. This focus will be justified post-hoc by the connection we are able to make with experimental observations. Given the small radial length scales of ETG modes, it is appropriate to use GENE in its local mode of operation, that is, running nonlinear simulations at a given flux surface and finding the heat flux. To more accurately reflect the heat flux flowing through the pedestal, we run a trio of

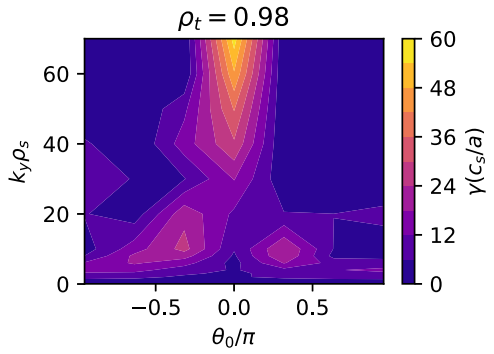

Figure 4. HPLG linear growth rate as a function of $k_y\rho_s$ and $\theta_0 = k_{x,\text{centre}}/\hat{s}k_y$ at $\rho_t = 0.98$. TETG modes at low $k_y\rho_s$ peak away from $\theta_0 = 0$.

simulations at different flux surfaces for each pulse and average the heat flux. Examining figure 1 and the upper row of figure 2, it is evident that the profiles are starkly different when plotted as functions of ρ_t, as the pedestal character changes between shots. Using a mtanh fitting function, we determine the approximate locations of the density pedestal top ($\rho_{t,n_{\text{e, ped}}}$) and temperature pedestal top ($\rho_{t,T_{\text{e, ped}}}$). We then use these to define three general flux surfaces which are:

A. Equidistant between $\rho_{t,n_{\text{e, ped}}}$ and $\rho_{t,T_{\text{e, ped}}}$: $\rho_t = \frac{\rho_{t,n_{\text{e, ped}}}+\rho_{t,T_{\text{e, ped}}}}{2}$ (i.e. at the top of the pressure pedestal),

B. $\rho_t = \rho_{t,n_{\text{e, ped}}}$ (i.e. at the top of the density pedestal),

C. Equidistant between $\rho_{t,n_{\text{e, ped}}}$ and the separatrix: $\rho_t = \frac{1+\rho_{t,n_{\text{e, ped}}}}{2}$ (i.e. in the steep gradient region of the pedestal).

The location of flux surfaces **A**, **B**, and **C** are displayed in figure 1 as circles, crosses, and squares respectively.

Before computing the heat flux using nonlinear simulations, we begin by examining ETG micro-instability at these three flux surfaces, using resolution parameters detailed in appendix A and again setting $T_\text{i} = T_\text{e}$. The results of these calculations are shown in figure 6, the top row of each panel displays the normalised linear growth rates, while the bottom row of each panel shows the real frequencies of the modes. As before, a seven-point scan in θ_0 is done for each $k_y\rho_s$ and the mode with the largest growth rate is plotted. The simulations at $\rho_t = \frac{\rho_{t,n_{\text{e, ped}}}+\rho_{t,T_{\text{e, ped}}}}{2}$ and $\rho_t = \rho_{t,n_{\text{e, ped}}}$ look qualitatively similar, the latter having slightly larger growth rates. At both of these flux surfaces, the normalised growth rates are similar for a given power regardless of the gas rate, and the normalised growth rates of the high power pulses are less than that of the low power pulses. The normalised growth rates on the steepest pressure gradient surface **C** are approximately a factor two larger than the other flux surfaces, and there are two primary peaks in the spectrum. The first, at $5 \lesssim k_y\rho_s \lesssim 20$ corresponds to pedestal TETGs, and the maximum growth rate is found when $\theta_0 \neq 0$ in all cases. The second peak at higher $k_y\rho_s$ comprises a myriad of sETG modes with different real frequencies. On these steep gradient region flux-surfaces, the high gas pulses both peak at lower $k_y\rho_s$ than the low gas pulses, which, as we shall see, has implications for turbulent heat transport due to ETGs at this flux surface.

Table 1. Minimum wavenumbers in the x-direction and maximum wavenumbers in the y-direction for the nonlinear flux tube simulations presented throughout. Other simulation parameters can be found in appendix A.

	$\frac{\rho_{t,n_{\text{e, ped}}}+\rho_{t,T_{\text{e, ped}}}}{2}$	$\rho_{t,n_{\text{e, ped}}}$	$\frac{1+\rho_{t,n_{\text{e, ped}}}}{2}$
$k_{x,\text{min}}\rho_s$	$\sim 0.67 - 1.3$	$\sim 0.67 - 1.3$	~ 1.3
$k_{y,\text{max}}\rho_s$	157.5	157.5	317.5–407.5

We now proceed to run nonlinear counterparts of the twelve linear simulations shown in figure 6. For all of the simulations, the velocity and parallel grids were set to the same as in the linear analysis (see appendix A), and we use $|k_{x,\text{max}}\rho_s| = 85$, and $k_{y,\text{min}}\rho_s = 2.5$. The chosen values of $k_{x,\text{min}}$ and $k_{y,\text{max}}$ for each flux surface are shown in table 1. Convergence tests in the simulation parameters have been carried out and are described here and in appendix A. The flux spectra for these twelve simulations as a function of $k_y\rho_s$ are shown in figure 7 and are plotted such that integrating over a given range of $k_y\rho_s$ corresponds to the total heat flux in that $k_y\rho_s$ range. For the two most radially inward flux surfaces **A** and **B**, the normalised flux spectra peak at approximately the same location, with the exception of the HPLG pulse which peaks at larger $k_y\rho_s$.

On the steepest gradient surface **C**, the LPLG pulse carries negligible ETG heat flux due to its comparatively low η_e value. Both high gas pulses have very similar flux spectra and therefore total normalised electron heat flux. The HPLG pulse peaks at higher $k_y\rho_s$ than the two high gas pulses but a significant fraction of the heat flux occurs at high $k_y\rho_s$. Linearly, modes at high $k_y\rho_s$ often possess a significantly larger parallel wavenumber k_z than their counterparts at lower $k_y\rho_s$. We note the area under both high power curves is approximately the same for both gas levels, meaning that the normalised heat flux is approximately the same for both pulses. The HPLG pulse has a larger Z_eff than its high gas counterpart, this leads to a stabilisation of ETGs and a reduction in the turbulent heat flux when the effect of impurities are included in the simulations (as they are throughout this section). For further details see appendix B.

The magnitude of the ETG turbulent heat flux $Q_{\text{e, ES}}$ in MW from these simulations is shown in figure 8 as blue bars for the low power pulses and red bars for the high power pulses. Also plotted as yellow bars in the same figures is the total neoclassical heat flux Q_NC (dominated by the ion component) calculated using NEO [35, 36]. Note that our assumption of $T_\text{i} = T_\text{e}$ (and hence $\omega_{T_\text{i}} = \omega_{T_\text{e}}$) means that Q_NC may be overestimated somewhat, particularly at flux surface **C**. Unsurprisingly, all three panels show that increases in power lead to increases in $Q_{\text{e,ES}}$; and increases in gas puffing result in moderate increases in turbulent heat flux for all high power pulses and the low power pulses at flux surface **C**. The lower panel of figure 8 shows that in the steep gradient region, Q_NC is the dominant heat flux channel in the LPLG case, and forms a significant fraction of the heat flux in the other cases, a feature that has been observed in multiple pulses within this dataset [28]. Across all flux surfaces, the HPHG pulses has the largest $Q_{\text{e,ES}}$

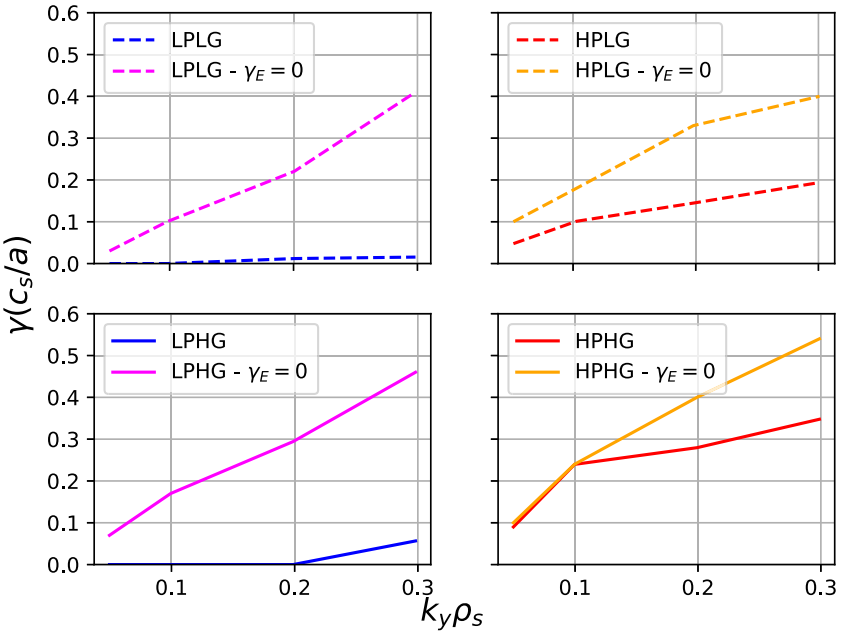

Figure 5. Growth rate spectra for our four pulses from global gyrokinetic simulations with and without equilibrium flow-shear. Shear stabilises ITG modes, particularly in the low power pulses which have lower $\omega_{T_\mathrm{i}} = \omega_{T_\mathrm{e}}$ and higher $|\gamma_{E\times B}|$ than their high power counterparts.

which is consistently larger than Q_{NC}. This provides strong evidence for ETG turbulence being responsible for the clamping of the ETG mid-way through the ELM cycle in this pulse [7].

To summarise and enable comparison with experiment, figure 9 plots $Q_{\mathrm{Tot}} = Q_{\mathrm{e,ES}} + Q_{\mathrm{NC}}$ for each shot. For the low gas pulses, power-balance analysis enables us to estimate the experimental pedestal heat flux Q_{EXP} [28]. We see that the combination of $Q_{\mathrm{e,ES}}$ and Q_{NC} allow us to match the experiment remarkably well, and a large fraction of the pedestal transport is attributable to ETG turbulence. For the high gas pulses, we are unable to estimate Q_{EXP} as the ELM frequency is too large for the power-balance analysis to be reliable [28]. Note, the experimental uncertainties in the temperature and density gradients can be significant in the pedestal, which may modify our answers somewhat. We have made no attempt to robustly capture the low $k_y\rho_s$ pedestal TETGs and sETGs in our nonlinear simulations. To do so would require a significantly smaller $k_{y,\mathrm{min}}\rho_s \sim 0.5$, and, due to the slower growth time of TETGs, the simulations would have to be run for much longer to ensure convergence [49].

4. Normalised temperature and density gradient scans

Having demonstrated the importance of ETG turbulence in our JET–ILW discharges, it is important to gain an understanding of how the level of turbulence responds to changes in the parameters that drive it. In this section, we focus specifically on the physics of ETG modes in transport barriers by considering the $\rho_t = \frac{1+\rho_{t,n_\mathrm{e,\,ped}}}{2}$ flux surface **C** only. To establish proximity to thresholds and understand the main mechanisms driving heat transport in JET–ILW pedestals, we perform scans in ω_{n_e} and ω_{T_e} around their nominal values for the HPHG case and display results in figures 10(*a*) and (*b*) respectively. The upper and lower panels of figure 10 display the growth rate and real frequency spectra respectively. Note that by performing these scans we are implicitly probing the experimental errors in our TS fitted profiles displayed in figure 1. In the ω_{n_e} scan, the peak growth rate no longer increases as η_e is increased via decreases in ω_{n_e} around the nominal value. Crucially, the spectrum moves to lower $k_y\rho_s$ as ω_{n_e} is decreased. This means for a given k_x, the mixing length estimate $\gamma/k_\perp^2$ would increase resulting in an increase in transport. Figure 10(*b*) shows different behaviour. The value of η_e is increased across the same range as figure 10(*a*), but by doing so via increases in ω_{T_e} the growth rates are increased in addition to decreases in $k_y\rho_s$. The traces that are the closest to the critical value for the onset of sETG modes $\eta_\mathrm{e} \sim 1$ [26, 50], show that the ω_{n_e} scan produces higher growth rates than the ω_{T_e} scan. However, while this pulse is subject to a similar η_e threshold as observed in references [26, 50], the green traces at $\eta_\mathrm{e} > 5$ show that this surface in the discharge is far above this threshold, with $\eta_\mathrm{e} \sim 4$, in a regime where the growth rate is sensitive to ω_{T_e} and relatively insensitive to ω_{n_e}. This likely represents a transition to more 'core-like' modes at low ω_{n_e} in that they are peaked at the outboard midplane. We use the term 'core-like', because despite the characteristics mentioned above, the modes owe their existence to large, pedestal-relevant values of ω_{T_e} and extreme shaping due to the pedestal geometry. In figure 10(*b*), the most extreme value of η_e in the scan (brown trace) displays an apparent mode transition in the vicinity of $k_y\rho_s \sim 150$. These are modes with such high parallel wavenumber that their eigenstructure cannot be satisfactorily resolved even with $n_z = 480$ grid-points, which leads to the growth rate of these modes being *slightly* over-predicted. This does not/will not affect any of the forgoing/following because: (i) the error in the over-predicted growth rate is negligible, (ii) even if it were

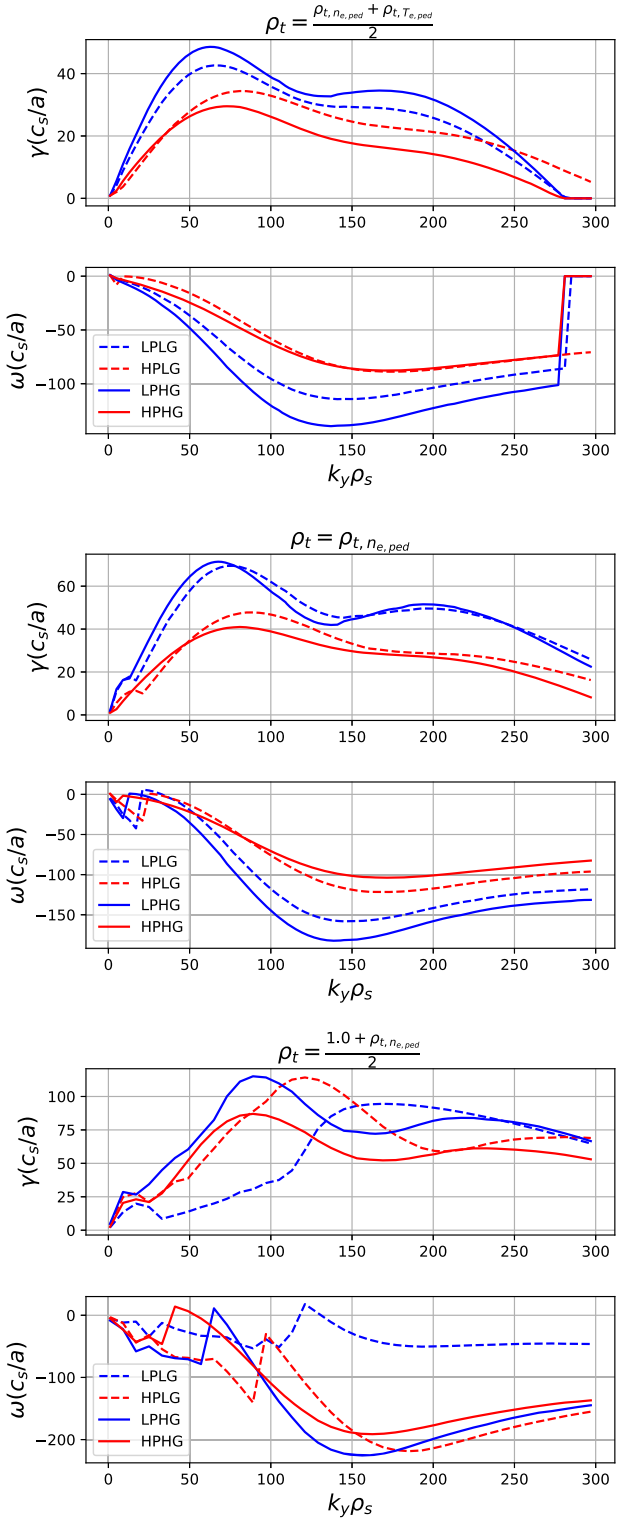

Figure 6. Growth rate spectra across our four pulses for three different generalised flux surfaces **A**, **B**, **C** displayed in left, middle, and right columns respectively. The colour of the traces and line-styles have the same meaning as in figures 1 and 2. Flux surfaces **A** and **B** show that the normalised growth rates in the low power pulses are larger than those of the high power pulses. The growth rates of the high gas pulses in flux surface **C**, the steep-gradient region, peak at lower $k_y\rho_s$ than the low gas growth rates.

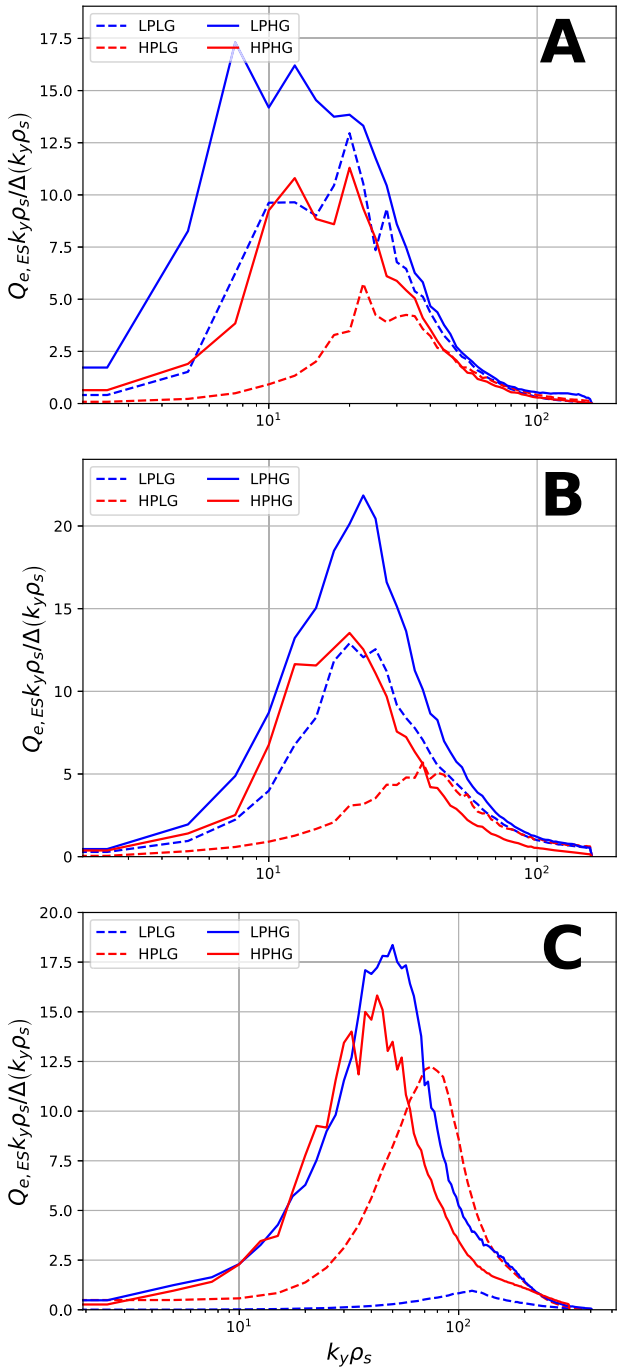

Figure 7. Heat flux spectra as a function of $k_y\rho_s$ for our four pulses at each of our three flux surfaces. From top to bottom the panels display results for flux surfaces **A**, **B**, and **C**. The colours and linestyles in each panel follow the same convention as previous figures. The units of the y-axis are normalised to gyro-Bohm units.

not, these modes exist at much higher $k_y\rho_s$ than the peak in the growth rate spectrum and therefore their contribution to the total heat flux is expected to be smaller than the contribution from modes at lower $k_y\rho_s$, and (iii) the problem only arises at $\omega_{T_e} \sim 40\%$ higher than nominal, so has little impact on nonlinear simulations of the experimental equilibrium.

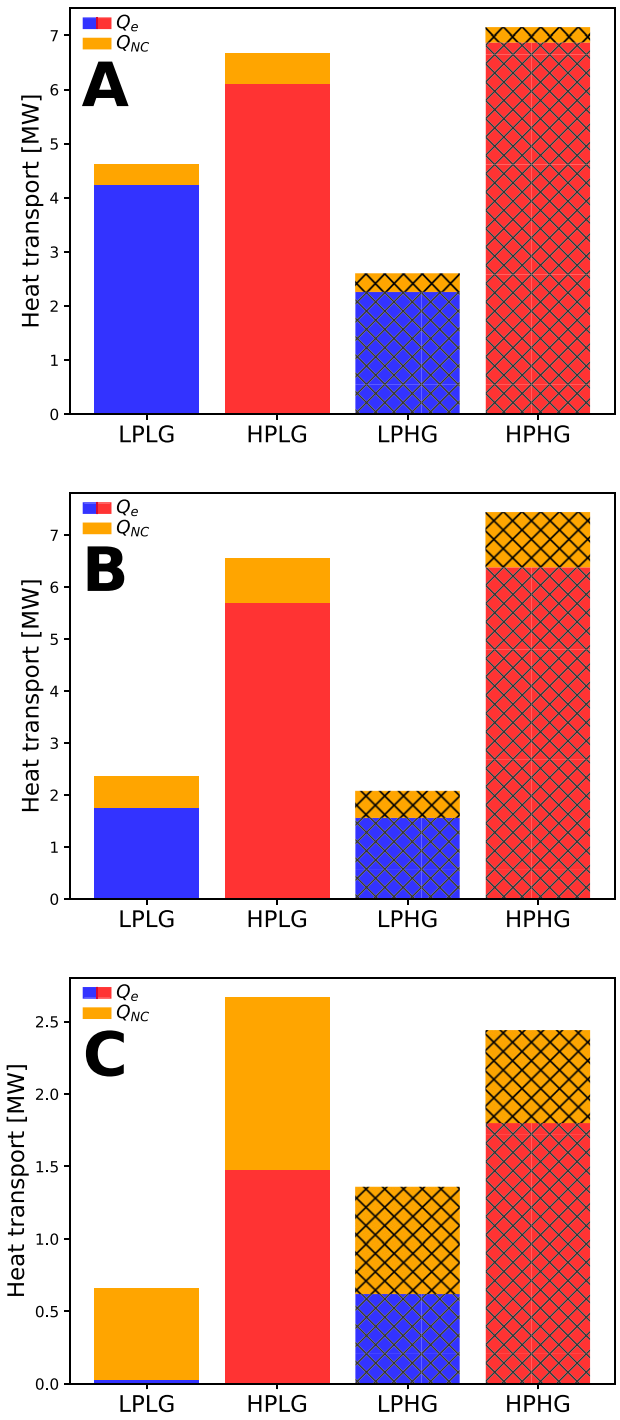

Figure 8. Blue and red bars: ETG heat flux in MW across our four pulses for each flux surface **A**–**C** (top to bottom). Corresponding the neoclassical heat flux (dominated by the ion component) is shown in the yellow bars. Thatched bars correspond to high gas pulses, while those without thatches correspond to low gas pulses.

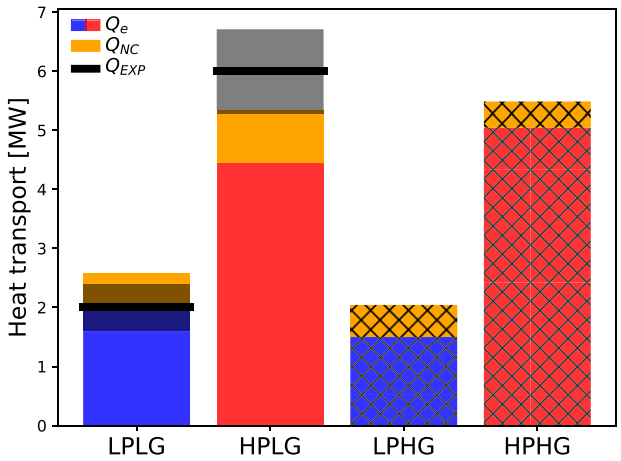

Figure 9. Average ETG turbulent (blue/red) and neoclassical heat flux (yellow) taken across the flux surfaces **A**–**C**. Thatched bars correspond to high gas pulses, while those without thatches correspond to low gas pulses. Black lines show the estimated power crossing the separatrix for the low gas pulses, along with a dark translucent region denoting the standard deviation in the data used in the power balance analysis [28].

Table 2. Nominal values of ω_{T_e}, ω_{n_e}, and $\eta_e = \omega_{T_e}/\omega_{n_e}$ for our four pulses.

	LPLG	LPHG	HPLG	HPHG
ω_{T_e}	31	34	43	25
ω_{n_e}	21	10	16	6
η_e	1.5	3.4	2.7	4.0

To obtain a macroscopic view of this among the four shots, for each shot we perform ω_{n_e} and ω_{T_e} scans across the same fractional increases in η_e and plot the peaks in the growth rate spectra such as those shown in figure 10 for each scan as a function of η_e/η_{e0} where η_{e0} is the nominal value. The results of this are shown in figure 11 (in which panel (d) corresponds to the data shown in figure 10), and a list of the (rounded) nominal values of $\omega_{T_e}, \omega_{n_e}$, and η_e for each shot is shown in table 2. In all cases, we see sharp increases in the peak growth rate associated with increases in η_e via decreases in ω_{n_e} at $\eta_e/\eta_{e,0} \ll 1$. The value of η_e at this critical point is $\sim$1 in all cases, corresponding to the well known threshold [26]. At the values of η_e in these discharges, which are well above threshold, and where $\eta_e/\eta_{e,0} \approx 1$, an increase in the peak growth-rate can only be achieved via an increase in ω_{T_e}. Thus, with perhaps the exception of the LPLG scans, at this general steep-gradient flux surface, our pulses have such small ω_{n_e} values that they are in an η_e regime far beyond the critical value where the growth rate is sensitive to ω_{T_e}, and relatively insensitive to ω_{n_e}. This is because, at low density gradient, the ETG growth rate is no longer sensitive to ω_{n_e} and is entirely determined by the fundamental drive from ω_{T_e}, which is constant in the ω_{n_e} scan. A similar effect has been observed for a variety of ITG eigenmodes in [51]. In this region of parameter space with low values of ω_{n_e} and high values of ω_{T_e}, the ETG turbulence displays a hybrid 'core-like' toroidal (due to magnetic curvature effects) and sETG character, which we will investigate in more detail in future work.

Having examined the linear response of ETGs to changing driving parameters, we now carry out a similar exercise to quantify the variation in the nonlinear turbulent heat flux and the level of stiffness in the high power pulses. In figure 12, we plot the heat flux in SI units against the fractional change in η_e from a series of nonlinear simulations at

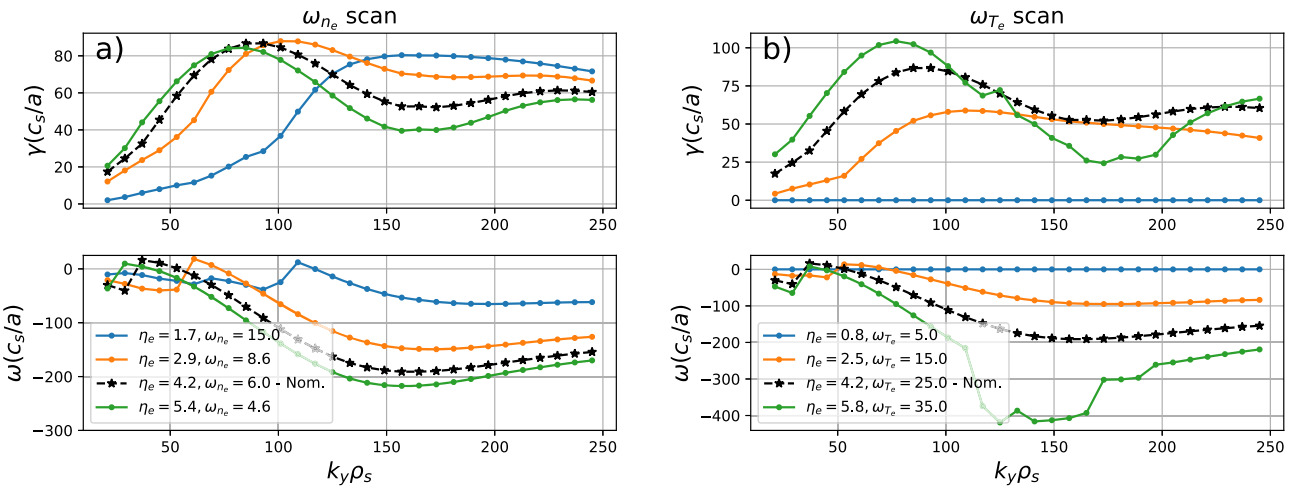

Figure 10. HPHG linear growth rate (top) and frequency (bottom) spectra as a function of poloidal wavenumber for several linear simulations with varying ω_{n_e} around its nominal value and at the nominal value of ω_{T_e} (a) and varying ω_{T_e} around its nominal value and at the nominal value of ω_{n_e} (b). The spectra for the nominal ω_{n_e} and ω_{T_e} are shown as black traces with star markers, and both panels scan the same range of η_e values. The legend displays the value of the scan parameter along with the associated value of $\eta_e = \omega_{T_e}/\omega_{n_e}$.

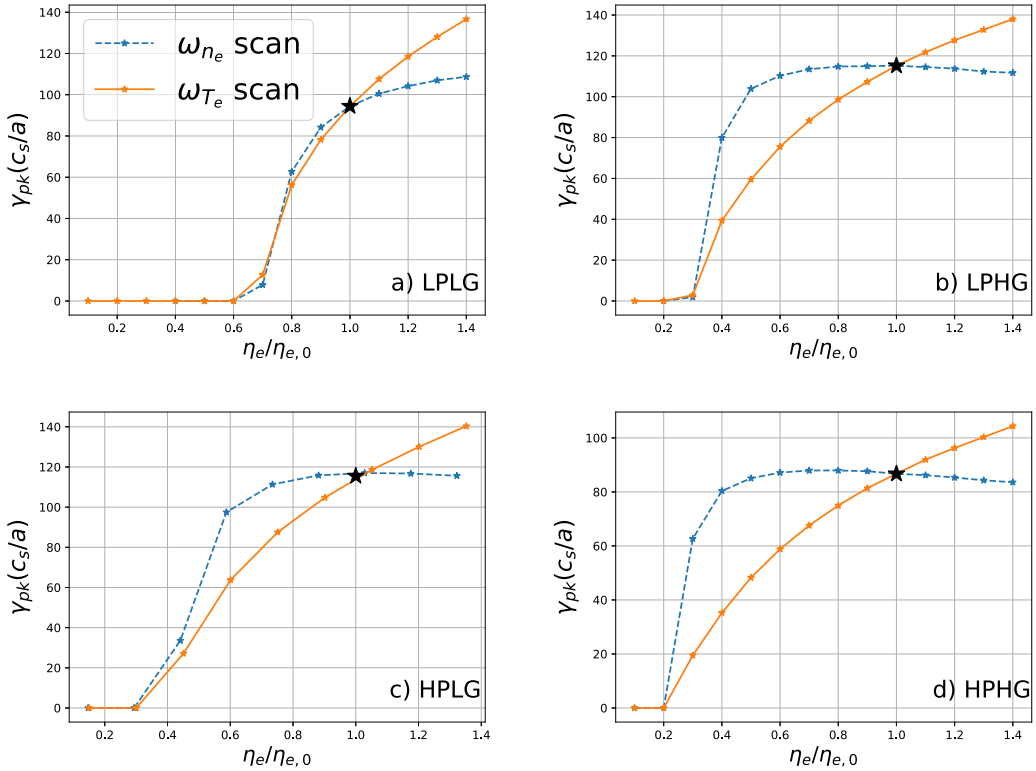

Figure 11. The peak in the growth rate spectrum γ_{pk} as a function of the normalised η_e in which ω_{n_e} (solid-orange) and ω_{T_e} (dashed-blue) have been scanned for each of our four pulses. The bottom right panel corresponding to the HPHG displays data shown in figure 10.

varying ω_{n_e} and ω_{T_e}. By plotting against the fractional change in the experimental value of η_e we are able to examine the qualitative changes in heat flux with ω_{T_e} and ω_{n_e} from two pulses with disparate flux spectra (see figure 7) and different values of η_e (see table 2). The solid and dashed black traces denote scans in ω_{T_e} and ω_{n_e} respectively. The data that comprises panel (a) was obtained using $n_z = 240$, while the data comprising panel (b) required $n_z = 480$, for reasons we discuss below. All simulations shown in figure 12 use two dynamic particle species only, with the role of impurities being limited exclusively to collisions via Z_{eff}. The two simulations at $\eta_e/\eta_{e,0} = 1$ are therefore the two-species counterparts of the red traces in the lower panel of figure 7, and the actual ETG heat flux is overestimated as a result. Including impurities in the following analysis is a worthwhile line of future enquiry, but we do not expect that it would qualitatively change the results of figure 12. To summarise the main observations of figure 12:

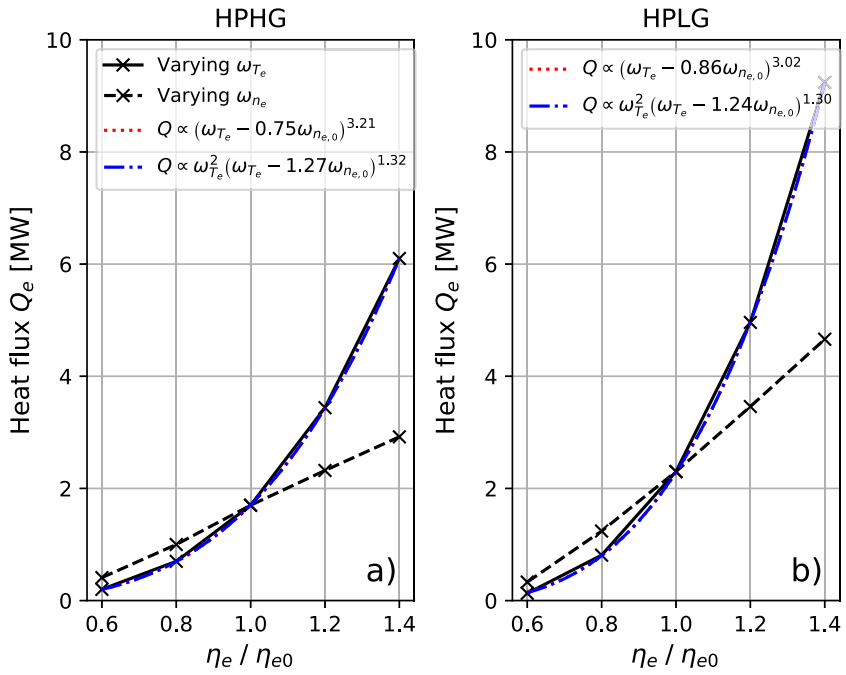

Figure 12. Heat flux due to ETG driven turbulent transport as a function of η_e/η_{e0} in the steep gradient region of two high power JET–ILW pulses with different gas rates. For each pulse, η_e is scanned around the nominal point using two methods: (i) increasing ω_{T_e} (solid black lines) and (ii) decreasing ω_{n_e} (dashed black lines). Blue and red (obscured) traces denote fits applied to the data comprising the ω_{T_e} scans (note the fractional change in ω_{T_e} is the same as the fractional change in η_e).

(a) Below the nominal value of η_e, the values of Q_e in SI units are slightly larger in the ω_{n_e} than they are in the ω_{T_e} scan. This is in agreement with the linear results plotted in the lower panels of figure 11, in which the peak in the growth rate spectrum is also larger in the ω_{n_e} scan than it is in the ω_{T_e} scan below the nominal η_e.

(b) Also in qualitative agreement with the linear results of figure 11, beyond the nominal η_e, larger Q_e variations are observed in the ω_{T_e} scans than in the ω_{n_e} scans.

(c) Transport increases steadily and approximately linearly as η_e is increased via ω_{n_e}.

(d) The variation in Q_e with ω_{T_e} is nonlinear in the ω_{T_e} scans.

We can draw upon linear results to interpret these nonlinear findings. Regarding point (iii), linear results show that despite the growth rate plateau as ω_{n_e} is decreased (figures 10(*a*) and 11), the growth rate spectrum moves to lower $k_y\rho_s$ (figure 10(*a*)). This means that provided the character of the eigenfunction is the same (i.e. it has similar k_x averaged over the field line), we would expect more heat transport due to a smaller k_y and therefore smaller $k_\perp$. Also shown in figure 12 are fits to the data comprising the ω_{T_e} scan using two different fitting functions:

$$Q_e \propto \left(\omega_{T_e} - \alpha\omega_{n_{e,0}}\right)^{\beta} \quad (1)$$

$$Q_e \propto \left(\omega_{T_e} - \delta\omega_{n_{e,0}}\right)^{\epsilon}\omega_{T_e}^2 \quad (2)$$

the use of which we will justify in the following. Equation (1) (equation (2)), α (δ) represents the threshold value of η_e for the onset of heat transport from sETG turbulence according to

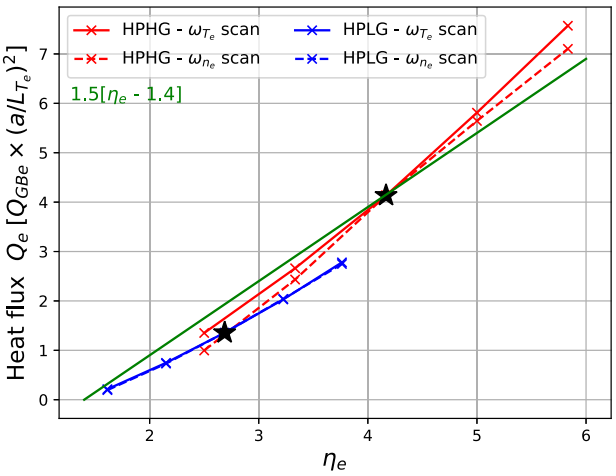

Figure 13. Normalised ETG heat flux as a function of η_e. Red and blue traces correspond to data from the HPHG and HPLG pulses respectively and black stars denote the operational points. For each pulse, η_e is scanned around the nominal point using two methods: (i) increasing ω_{T_e} (solid lines) and (ii) decreasing ω_{n_e} (dashed lines). The heat flux is normalised to the modified electron gyro-Bohm heat flux which uses the temperature gradient length L_{T_e} in the normalisation. The solid green line shows the trend $Q_e/Q_{GBe} = 1.5\,[\eta_e - 1.4]$, details of which can be found in reference [50].

$\omega_{T_{e,cr}} = \eta_{e,cr}\omega_{n_{e,0}}$, while $\omega_{n_{e,0}}$ denotes the nominal value of ω_{n_e} which can be found in table 2. Equation (1) gives critical values of $\eta_{e,cr} \equiv \alpha = 0.75 \pm 0.06$ and $\eta_{e,cr} \equiv \alpha = 0.86 \pm 0.09$ for the HPHG and HPLG ω_{T_e} scans respectively. These values are in excellent agreement with each other, and are consistent with the linear thresholds shown in figure 11 and reference [26].

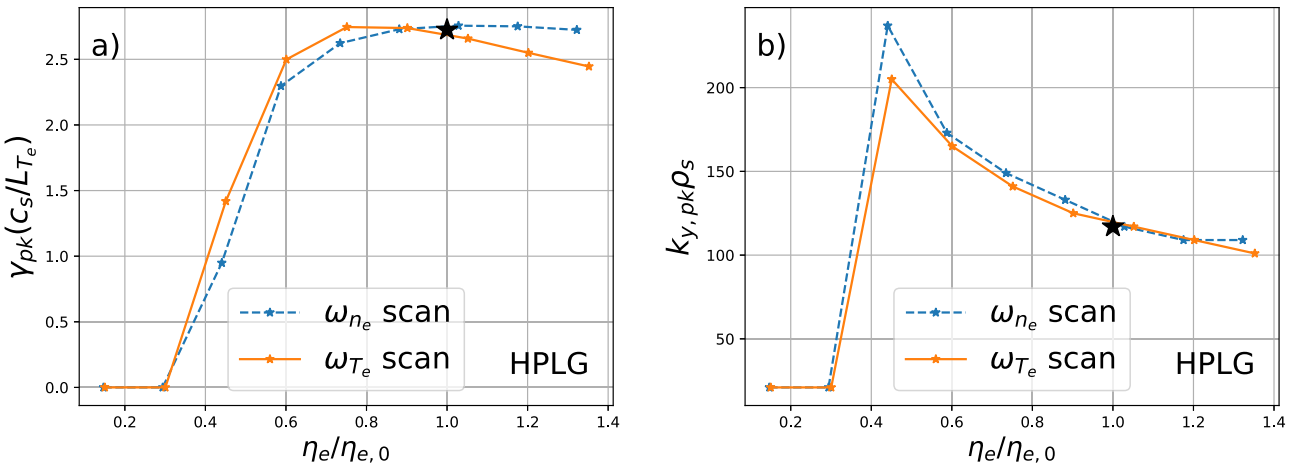

Figure 14. (*a*) The peak in the growth rate spectrum γ_{pk} normalised using the temperature scale length L_{T_e} as a function of the normalised η_e in which ω_{n_e} (solid-orange) and ω_{T_e} (dashed-blue) have been scanned around their nominal values in the HPLG pulse. (*b*) The value of $k_y\rho_s$ for which the growth rate peaks as a function of normalised η_e for an ω_{n_e} scan and a ω_{T_e} scan around the equilibrium values of the HPLG pulse. Data corresponds to that shown in figure 11(*c*) and is qualitatively the same for all four pulses. The apparent discontinuity at $\eta_e/\eta_{e,0} = 0.2$ is due to the modes with $\eta_e \lesssim 1$ being stable, see figure 11.

The exponents of equation (1) are $\beta = 3.21 \pm 0.05$ and $\beta = 3.02 \pm 0.12$ for the HPHG and HPLG ω_{T_e} scans respectively and are again in excellent agreement with one another. Under the condition $\omega_{T_e} \gg \omega_{T_{e,\,cr}} = \eta_{e,\,cr}\omega_{n_{e,0}}$, i.e. well above marginality, equation (1) would approximately reduce to $Q_e \approx \omega_{T_e}^3$ for both pulses, which is close to the scaling predicted theoretically for core ITG turbulence well above threshold using the critical balance hypothesis [41, 42].

Using equation (2) as the fitting function results in $\eta_{e,cr} \equiv \delta = 1.27 \pm 0.09$ and $\eta_{e,cr} \equiv \delta = 1.24 \pm 0.05$ for HPHG and HPLG respectively, while the exponent is $\epsilon = 1.32 \pm 0.04$ and $\epsilon = 1.30 \pm 0.03$ for the HPHG and HPLG ω_{T_e} scans respectively. As ϵ deviates only slightly from a linear dependence, it is clear that the fits using both parameterisations in equations (1) and (2) reduce to $Q_e \approx \omega_{T_e}^3$ for these pulses when $\omega_{T_e} \gg \omega_{T_{e,\,cr}} = \eta_{e,\,cr}\omega_{n_{e,0}}$. Both the threshold values of $\eta_{e,cr} \equiv \delta$ and the weakly nonlinear exponents ϵ are in good agreement with reference [50], which we now discuss.

The fits to equations (1) and (2) are overlaid in figure 12 where the former has been obscured by the latter but is still retained in the figure legend. These fits are not normalised whereas in reference [41], the core ITG ion heat flux is normalised to the ion gyro-Bohm heat flux, Q_{GBi} using the major radius R as the normalising equilibrium length scale. In figure 13 we replot the data displayed in figure 12 in electron gyro-Bohm units but instead using the temperature gradient scale length L_{T_e} as the relevant scale length in the normalisation. Henceforth, we reserve the notation Q_{GBe} to refer to the 'core' gyro-Bohm factor which uses the macroscopic scale length (the minor radius a in this case), and Q_{MGBe} to refer to a modified gyro-Bohm factor which uses the temperature gradient scale length L_{T_e} which is more appropriate in the steep gradient region of the pedestal. Figure 13 shows that Q_e/Q_{MGBe} has an approximately linear dependence on η_e in both the ω_{n_e} and ω_{T_e} scans for both pulses. This is consistent with our fits to the electron heat flux dependence on ω_{T_e} using equation (2), which can be recast to use η_e as the independent variable, to give:

$$Q_e/Q_{GBe} \propto \left(\eta_e - \eta_{e,\,cr}\right)\omega_{T_e}^2; \tag{3}$$

where we have approximated $\epsilon \sim 1$ and normalised the flux by Q_{GBe}, which is constant throughout the scans. Dividing both sides of equation (3) by $\omega_{T_e}^2$ results in linear scaling gives $Q_e/Q_{MGBe} \propto \eta_e - \eta_{e,cr}$, irrespective of whether ω_{T_e} is scanned at constant ω_{n_e} or ω_{n_e} is scanned at constant ω_{T_e}. All four scans across the two pulses display approximately the same nearly linear dependence of the heat flux (appropriately normalised) on η_e. Gyrokinetic simulations of ETG turbulence close to threshold ($1 \lesssim \eta_e \lesssim 2.5$) in DIII–D pedestals have been shown in reference [50] to fit the expression $Q_e/Q_{MGBe} = 1.5\,[\eta_e - 1.4]$. This is in close agreement with the fits to JET–ILW pedestal data in this paper using equation (2). Our results are therefore consistent with this model, showing only moderate differences in the gradient of the graphs (related to the profile stiffness) among our two pulses. It is also interesting to note the role that increased gas puffing has on the heat flux at the operational point when using this normalisation—increasing the gas moves the pulse up the approximately linear Q_e/Q_{MGBe} vs η_e curve. While the heat flux in MW is the same for the HPLG and HPHG pulses in the steep gradient region (see figure 8(*C*)), the normalised steep gradient heat flux (with L_{T_e} as the scale length) is approximately four times larger in the HPHG than in the HPLG case. We note that our data range $1 \lesssim \eta_e \lesssim 6$ exceeds the $\eta_e \lesssim 2.5$ data range used in reference [50] and, unlike reference [50], we have not carried out any nonlinear simulations close to the critical threshold.

The results presented in figure 13 show that variations in η_e via ω_{n_e} and ω_{T_e} produce nearly identical trends in the normalised turbulent heat flux. This appears to be inconsistent with the linear results presented in figure 11, in which the ω_{n_e} and ω_{T_e} scans produce different trends. To resolve this apparent inconsistency, figure 14(*a*) replots the HPLG peak linear

growth rate data shown in figure 11(*c*), but instead using L_{T_e} as the scale length in the growth rate normalisation. The differences in the peak growth rate trends between the ω_{T_e} and ω_{n_e} scans are now less pronounced, with the scans showing similar trends until η_e exceeds $\eta_{e,0}$. In the ω_{T_e} scan, as η_e is increased above η_0 (by raising ω_{T_e}), the normalised peak growth rate actually starts to decrease slightly, whereas in the ω_{n_e} scan, the peak growth rates saturate as η_e is increased by reducing ω_{n_e}. In figure 14(*b*) we also plot the trend in the value of $k_y\rho_s$ for which the HPLG growth rate peaks as a function of $\eta_e/\eta_{e,0}$. This is also near-identical for η_e variation via either ω_{n_e} or ω_{T_e}. This strongly suggests that it is η_e that determines the location of the peaks in the turbulent heat flux spectra shown in the lower panel of figure 7; indeed, the peaks in the lower panel of figure 7 can be ordered from right to left in increasing η_e. This distinctive dependence of the spectrum on η_e is a key component of a new quasilinear model of ETG pedestal turbulence described in [38]. While the corresponding traces for the other three pulses are not shown, the trend is qualitatively similar. The mode structures (not shown) are similar in both scans, meaning the value of $k_\perp$ is also the same between the two scans and follows a similar trend to that shown in figure 14(*b*). Coupled with the similar growth rate trends shown in figure 14(*a*), this results in the two scans having similar mixing length estimates $\sim \gamma/k_\perp^2$, and therefore similar levels of transport. Thus, taken together, these two results allow us to establish a strong link between linear ETG microinstability simulations and nonlinear turbulence simulations. While there are certainly more subtleties to this logic that should be explored in more detail, figure 14 nevertheless provides valuable insight for the development of future reduced models of ETG turbulence in the pedestal.

5. Discussion and conclusions

Using local gyrokinetic simulations, we have examined the impact of ETG modes on turbulent transport in four JET–ILW discharges with varying levels of input power and gas fuelling. For each of the four pulses, we have examined the linear stability and nonlinear turbulence associated with ETG modes at three different flux surfaces from the top of the pressure pedestal to the steep gradient region. We found that large binormal wavenumbers $k_y\rho_s$ along with many grid points in the parallel direction were necessary to accurately compute both linear growth rates and nonlinear heat fluxes. The sum of ETG turbulent heat flux and neoclassical heat flux computed using NEO were able to successfully (within the broad error bars of experiment) match the power crossing the separatrix for the low gas pulses. We were unable to get an estimate of Q_{EXP} for the high gas pulses due to the large ELM frequency [28], but we believe it is likely that the combination of ETG and neoclassical heat flux also contributes a large fraction of the heat transport for these cases.

We then performed linear scans of the normalised temperature gradient ω_{T_e} and the normalised density gradient ω_{n_e} for each of the four pulses, demonstrating that these pedestals have values of η_e far above the critical value for the onset of sETG modes [26]. Rather, they are in a regime in which the linear stability of these modes is more sensitive to changes in ω_{T_e} than changes in ω_{n_e}. Despite this observation, the value of $k_y\rho_s$ for which the linear growth rate spectrum peaks was determined by η_e in all four cases, with higher values of η_e leading to lower values of $k_y\rho_s$. This is also consistent with the steep gradient nonlinear flux spectra presented here, and is a key component of a new quasilinear model of ETG pedestal turbulence described in [38]. Corresponding nonlinear scans in ω_{T_e} and ω_{n_e} for the two high power pulses showed similarities with trends in the peak growth rates from linear simulations. Below the nominal gradient values, increases in η_e via decreases in ω_{n_e} produced larger peak growth rates and heat fluxes than increases in η_e via increases in ω_{T_e}. The opposite was true above the nominal gradient values, with the ω_{T_e} scan producing larger heat fluxes and growth rates, the former increasing dramatically as ω_{T_e} is increased and displays evidence of critical balance [41, 42]. We then renormalised our nonlinear heat flux data in units of the modified electron gyro-Bohm heat flux using the temperature gradient scale length L_{T_e}. With this normalisation, the changes in heat flux with ω_{T_e} and ω_{n_e} were very similar for the HPHG pulse, and nearly identical for the HPLG pulse, resulting in a general trend of normalised heat flux increasing with η_e. The trends in this normalised heat flux with η_e were similar among the two pulses, and were in broad agreement with the scaling reported from gyrokinetic analysis of ETG turbulence in DIII–D pedestals [50]. Figure 12 shows that at the smallest values of η_e simulated, there is negligible turbulent heat flux due to ETG modes. This corresponds to plasmas with large values of ω_{n_e} (or equivalently small values of ω_{T_e}), which is broadly the regime of JET–C pedestals (see, for example, figure 12 of reference [25]). Indeed, the simulations presented in reference [25] showed that when the relative shift between the density and temperature pedestals is increased (producing a decrease in ω_{n_e} and therefore an increase in η_e) from values representative of JET–C to values representative of JET–ILW, the ETG linear growth rates and turbulent heat flux increases dramatically.

An important result of this paper is the comparison between the HPHG and HPLG flux spectra shown in figure 7(*C*). We have shown that the normalised steep gradient heat flux (with L_{T_e} as the scale length) is approximately four times larger in the HPHG than in the HPLG case, while both pulses have similar total heat flux in physical units. Simulations presented here and in previous works have shown that sETG turbulent heat flux increases as η_e increases, our simulations extend this work by exploring in more detail what happens well above the η_e threshold as we push to higher ω_{T_e} values.

The primary results of this work can be succinctly summarised as follows:

- The heat flux from single scale ETG simulations combined with neoclassical simulations is in remarkably good agreement with estimates of the experimental heat flux for the two low power pulses, and is likely the dominant transport mechanism in the high gas pulses as well.
- $\eta_e = \omega_{T_e}/\omega_{n_e}$ is an important parameter which characterises the location of the peak in the ETG growth rate and heat flux spectra.

- In the steep gradient region of the pedestal and at density and temperature gradients exceeding experimental values, the largest increases in growth rate and heat flux in SI units comes from increases in ω_{T_e}.
- There is a strong increase in Q_e as ω_{T_e} increases above the experimental point, suggesting that ETGs limit the temperature gradient in these pulses in strong support of experimental observations [7].
- When the heat flux from the ω_{T_e} and ω_{n_e} scans is plotted in electron gyro-Bohm units using the temperature gradient scale length L_{T_e} as the equilibrium scale length, both scans and both pulses follow a similar trend with η_e, which agrees well with the model of reference [50].

Throughout this paper, we have tried to be candid with regards to the challenges and shortcomings of our simulations, particularly with regards to resolution in the parallel direction. An awareness of these issues is vital if we are to be able to improve our understanding of ETG turbulent heat transport in the pedestal. As an example, when comparing two linear ETG spectra, it may be tempting to suppose that a spectrum that peaks at lower $k_y\rho_s$ must have a larger mixing length estimate $\chi \sim \gamma/k_\perp^2$ and therefore must carry more heat flux. Figures 6 and 7 demonstrate that such an assumption would be flawed for the high power pulses at flux surface **C** as there exists modes with large k_z at high $k_y\rho_s$ which contribute a significant fraction of the heat flux. This leads to the two pulses having similar dimensional heat flux levels despite peaking at significantly different values of $k_y\rho_s$.

Despite our simulations encompassing a large range of physical effects and length scales vital for comparison with experiment; the 30+ nonlinear simulations and associated resolution testing required for this study necessitated the exclusion of some possibly important physical effects. One such effect is the interaction between ETG modes and MTMs in the pedestal which was presented in reference [52]. This was not included in our electron scale nonlinear simulations as our minimum resolvable wavenumber was $k_y\rho_s$ and MTMs generally peak at $k_y\rho_s \sim O\left(10^{-1}\right)$; see, for instance, section 2.[5] We also made no attempt to robustly capture $k_y\rho_s \sim 1$ ETGs in our steep-gradient nonlinear simulations and the linear simulations presented in section 3 onwards which are restricted to $\theta_0 = 0$ [20]. To do so would require a significantly smaller $k_{y,\min}\rho_s \sim 0.5$, and the simulations would have to be run for much longer to ensure convergence due to the slower growth time of TETGs and sETGs that peak away from the outboard midplane [49]. This was achieved in reference [49], the trade off being the absence of electro-magnetic effects and dynamic impurity species, as well as the use of strong hyper-diffusion to damp modes at large $k_y\rho_s$. The steep-gradient region sETG turbulent heat flux reported in the steep-gradient simulations here required large values of n_z and $k_{y,\max}$, thus, to adequately resolve the sETGs reported here along with off-midplane ETGs would be an immensely challenging multi-scale problem in all three spatial coordinates x, y, and z.

While this manuscript finds many points of intersection with the works of [49, 52], none of these three works have attempted to simultaneously capture: (i) multi-scale interactions with MTMs, (ii) ETG turbulent heat-flux that peak at locations other than the outboard midplane, (iii) high k_z sETGs such as those studied here, and (iv) the stabilising effect of impurities. Future investigations of points (i)–(iv) simultaneously would make for an enthralling study, but a thorough understanding of each of these things in isolation and placing them firmly in the context of experimental observations must be the first step.

[5] We note that in reference [52] the simulations were unable to model the interaction on the growth time-scale of the MTM, however, and the parallel grids may have been insufficient to resolve the high parallel wavenumber sETGs reported here (but were locally converged in parallel grid resolution).

Acknowledgments

The authors thank T. Görler for informative discussions. This work was supported by US DOE Contract No. DE-FG02-04ER54742 and US DOE Office of Fusion Energy Sciences Scientific Discovery through Advanced Computing (SciDAC) program under Award No. DE-SC0018429. This work has been carried out within the framework of the EUROfusion Consortium and has received funding from the Euratom research and training programme 2014–2018 and 2019–2020 under Grant Agreement No. 633053 and from the RCUK [Grant Number EP/T012250/1]. To obtain further information on the data and models underlying this paper please contact PublicationsManager@ukaea.uk. The views and opinions expressed herein do not necessarily reflect those of the European Commission.

Appendix A. Simulation parameters

Three particle species were used throughout all the local and global linear simulations presented in this manuscript. The third species was assumed to be a dominant beryllium impurity, and its contribution included in the equilibrium self-consistently using the best available estimates of the effective charge Z_{eff}. Three species were also used in all nonlinear simulations presented in section 3 for the comparison to experimental heat fluxes. The nonlinear normalised temperature and density gradient scans presented in the latter half of section 4 used two particle species, and instead partially included the effects of impurities by specifying Z_{eff} which enters into the collision operator.

A.1. Local linear GENE simulations

For the local linear simulations presented throughout the parallel velocity domain spanned $|l_{v_{\text{parallel}}}| = 3v_{\text{TD}}$ using $n_{v_\parallel} = 36$ grid-points and the magnetic moment co-ordinate was from 0 to 9 using 16 grid points. Convergence tests were carried out increasing both the ranges and the number of grid-points and no appreciable difference in the linear growth rates were found. We used $n_{k_x} = 13$ connected flux-tubes in all linear simulations, and a minimum of $n_z = 240$ parallel grid points

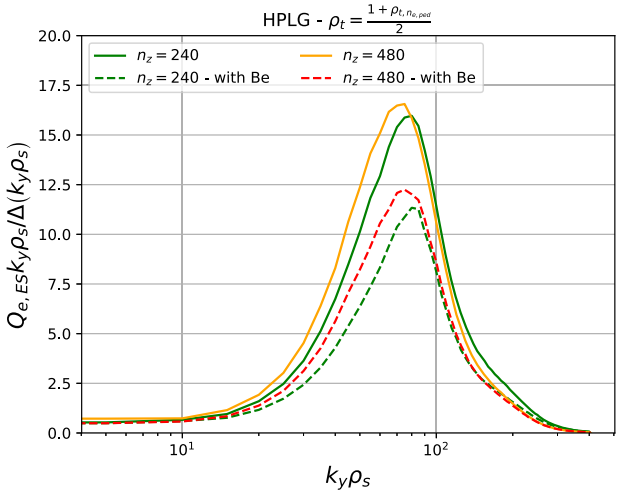

Figure B1. Heat flux spectra as a function of $k_y\rho_s$ for the HPLG pulse at flux surface **C**. Dashed (solid) traces correspond to simulations in which beryllium is (is not) included in the simulation as a dynamic impurity species. The green traces correspond to simulations with $n_z = 240$ grid points while the orange and red traces correspond to simulations with $n_z = 480$ grid points. The dashed red trace is identical to that shown in figure 7(*C*).

were used in all simulations (note that $n_z = 240$ is probably more than is needed for the two most radially inward flux surfaces). For some ETG simulations at values of normalised temperature gradient significantly above the nominal, $n_z = 480$ was required to resolve slab modes with a lot of parallel structure. All simulations used collisions providing natural velocity space dissipation so only a modest value of parallel hyper diffusion $hypv = 0.2$ was used. In the parallel direction $hypz = -1$ was used.

A.2. Local nonlinear GENE simulations

The velocity domains were the same as in the linear simulations but $n_\mu = 8$ grid points were used. We used $240 \leqslant n_z \leqslant 480$ for our convergence testing and discuss this in more detail in the main text along with the resolution in the x and k_y directions. In the parallel velocity direction $hypv = 0.2$ was again used and the parallel hyperdiffusion strength was increased to $hypz = -2$. In 11 of the 12 simulations presented in section 3, no hyperdiffusion was used in the x and k_y directions (hence the large $k_{y,\max}$ values, discussed in the main text). The exception to this was the HPLG simulations presented in figure B1 and the dashed-red trace in figure 7(*C*). These simulations, and those presented in section 4, used small levels of hyperdiffusion in the x and k_y directions provided by the GENE's GyroLES adaptive hyper-diffusion algorithm [53].

A.3. Global linear GENE simulations

The global simulation parameters are as follows:

- $|l_{v_{\text{parallel}}}| = 4v_{\text{TD}}$ with $n_{v_\parallel} = 64$
- $0 \leqslant \mu \leqslant 11$ using $n_\mu = 24$
- $n_x = 320$
- $n_z = 84$
- $hypv = 0.2$
- $hypx = 1.0$
- $hypz = -3$

A.4. NEO neoclassical simulations

NEO input files were prepared with three species (Be as the intrinsic impurity), assuming equal electron and ion temperatures and selecting the default full linearised Fokker–Planck collision operator. General Grad–Shafranov geometry specified with Fourier coefficients were used. Default values for the numerical resolution were applied: $N_\theta = 17$ for the number of poloidal grid points, $N_\xi = 17$ for the number of ξ-polynomials ($\xi = v_\parallel/v$ is the cosine of the pitch angle) and $N_x = 6$ for the number of energy polynomials in the computational domain.

Appendix B. The effect of impurities on ETG modes

The effect of dynamic impurities on the heat flux is investigated in figure B1 for the HPLG pulse at the steep gradient flux surface **C**. The dashed traces display the results of simulations in which, like the rest of the simulations in this section, a beryllium impurity was included as a third dynamic species; while the solid traces correspond to two-species simulations which instead specified $Z_{\text{eff}} = 1.66$ and therefore only partially model impurities via collisions. In both cases the equilibrium is kept fixed, any small changes in the equilibrium are expected to play a minor role here. Also shown in figure B1 is the effect of doubling the parallel resolution both with and without dynamic impurities. The green traces display results using $n_z = 240$ while the yellow and red traces use $n_z = 480$. The red-dashed trace is identical to that shown in the bottom panel of figure 7. Strikingly, we see that even for this low value of Z_{eff} (compared to a typical JET–C value), neglecting impurities over-estimates the heat flux by $\sim$36% regardless of the n_z resolution. The stabilising effect on ETG turbulence when using dynamic impurities arises from their contribution to the adiabatic ion response which reduces the instability drive [54]. This has also been demonstrated in [26] where it is also captured as an effect in the critical gradient formula contained within. This stabilising effect of impurities may be contribute to the improved pedestal performance seen with moderate nitrogen seeding on JET–ILW [6, 10, 11]. We note that the HPLG pulse for which we have demonstrated this effect has the highest Z_{eff} of our four pulses, therefore stabilisation of ETG modes via impurities is expected to play less of a role for the other three pulses. Figure B1 also shows that doubling n_z increases the total heat flux and downshifts the k_y spectrum very slightly, with an 11% increase in the three species cases and a $\sim$7% increase in the two species cases. Similarly small increases in heat flux with increasing n_z were observed for the other pulses, and we can

therefore proceed confident that the results presented in this section are converged.

ORCID iDs

B. Chapman-Oplopoiou https://orcid.org/0000-0001-9879-2285
D.R. Hatch https://orcid.org/0000-0002-1625-4385
A.R. Field https://orcid.org/0000-0003-0671-9668
L. Frassinetti https://orcid.org/0000-0002-9546-4494
L. Horvath https://orcid.org/0000-0002-5692-6772
C.F. Maggi https://orcid.org/0000-0001-7208-2613
J.F. Parisi https://orcid.org/0000-0001-8701-439X
C.M. Roach https://orcid.org/0000-0001-5856-0287
S. Saarelma https://orcid.org/0000-0002-6838-2194
J. Walker https://orcid.org/0000-0003-4345-2624

References

[1] Wagner F. *et al* 1982 *Phys. Rev. Lett.* **49** 1408–12
[2] Matthews G.F. *et al* 2011 *Phys. Scr.* **T145** 014001
[3] Beurskens M.N.A. *et al* 2013 *Plasma Phys. Control. Fusion* **55** 124043
[4] Joffrin E. *et al* 2013 *Nucl. Fusion* **54** 013011
[5] Leyland M. *et al* 2014 *Nucl. Fusion* **55** 013019
[6] Maggi C. *et al* 2015 *Nucl. Fusion* **55** 113031
[7] Maggi C. *et al* 2017 *Nucl. Fusion* **57** 116012
[8] Frassinetti L. *et al* 2016 *Nucl. Fusion* **57** 016012
[9] Frassinetti L. *et al* 2019 *Nucl. Fusion* **59** 076038
[10] Giroud C. *et al* 2013 *Nucl. Fusion* **53** 113025
[11] Giroud C. *et al* 2015 *Plasma Phys. Control. Fusion* **57** 035004
[12] Hatch D., Kotschenreuther M., Mahajan S., Valanju P., Jenko F., Told D., Görler T. and Saarelma S. 2016 *Nucl. Fusion* **56** 104003
[13] Hatch D., Kotschenreuther M., Mahajan S., Valanju P. and Liu X. 2017 *Nucl. Fusion* **57** 036020
[14] Hatch D. *et al* 2019 *Nucl. Fusion* **59** 086056
[15] Hatch D. *et al* (JET Contributors) 2021 *Nucl. Fusion* **61** 036015
[16] Larakers J.L., Curie M., Hatch D.R., Hazeltine R.D. and Mahajan S.M. 2021 *Phys. Rev. Lett.* **126** 225001
[17] Kotschenreuther M., Hatch D., Mahajan S., Valanju P., Zheng L. and Liu X. 2017 *Nucl. Fusion* **57** 064001
[18] Kotschenreuther M. *et al* 2019 *Nucl. Fusion* **59** 096001
[19] Bowman C. *et al* 2017 *Nucl. Fusion* **58** 016021
[20] Parisi J.F. *et al* (JET Contributors) 2020 *Nucl. Fusion* **60** 126045
[21] Hassan E., Hatch D.R., Guttenfelder W., Chen Y. and Parker S. 2021 *Phys. Plasmas* **28** 062505
[22] Stefanikova E. *et al* 2018 *Nucl. Fusion* **58** 056010
[23] Stefanikova E., Frassinetti L., Saarelma S., von Thun C.P. and Hillesheim J. (JET Contributors) 2020 *Nucl. Fusion* **61** 026008
[24] Walker J. and Hatch D.R. 2022 in preparation
[25] Frassinetti L. *et al* (JET Contributors) 2021 *Nucl. Fusion* **61** 126054
[26] Jenko F., Dorland W. and Hammett G.W. 2001 *Phys. Plasmas* **8** 4096–104
[27] Görler T., Lapillonne X., Brunner S., Dannert T., Jenko F., Merz F. and Told D. 2011 *J. Comput. Phys.* **230** 7053–71
[28] Field A.R. *et al* 2020 *Plasma Phys. Control. Fusion* **62** 055010
[29] Frassinetti L., Beurskens M.N.A., Scannell R., Osborne T.H., Flanagan J., Kempenaars M., Maslov M., Pasqualotto R. and Walsh M. 2012 *Rev. Sci. Instrum.* **83** 013506
[30] Simpson J., Moulton D., Giroud C., Groth M. and Corrigan G. 2019 *Nucl. Mater. Energy* **20** 100599
[31] Landreman M. and Ernst D.R. 2012 *Plasma Phys. Control. Fusion* **54** 115006
[32] Viezzer E. *et al* 2013 *Nucl. Fusion* **53** 053005
[33] Huysmans G.T.A., Goedbloed J.P. and Kerner W.O.K. 1991 Isoparametric bicubic hermite elements for solution of the Grad–Shafranov equation *Proc. CP90 Conf. on Computational Physics* (Amsterdam, The Netherlands September 1990)
[34] Hager R. and Chang C.S. 2016 *Phys. Plasmas* **23** 042503
[35] Belli E.A. and Candy J. 2008 *Plasma Phys. Control. Fusion* **50** 095010
[36] Belli E.A. and Candy J. 2011 *Plasma Phys. Control. Fusion* **54** 015015
[37] von Thun C.P. *et al* 2019 *Nucl. Fusion* **59** 056004
[38] Hatch D.R. *et al* 2022 *Phys. Plasmas* **29** 6
[39] Redl A., Angioni C., Belli E. and Sauter O. 2021 *Phys. Plasmas* **28** 022502
[40] Told D., Jenko F., Xanthopoulos P., Horton L.D. and Wolfrum E. 2008 *Phys. Plasmas* **15** 102306
[41] Barnes M., Parraf F.I. and Schekochihin A.A. 2011 *Phys. Rev. Lett.* **107** 115003
[42] Adkins T., Schekochihin A.A., Ivanov P.G. and Roach C.M. 2022 in preparation
[43] Saarelma S., Martin-Collar J., Dickinson D., McMillan B.F. and Roach C.M. 2017 *Plasma Phys. Control. Fusion* **59** 064001
[44] Collar J.P.M., McMillan B.F., Saarelma S. and Bottino A. 2020 *Plasma Phys. Control. Fusion* **62** 095005
[45] Hager R., Lang J., Chang C.S., Ku S., Chen Y., Parker S.E. and Adams M.F. 2017 *Phys. Plasmas* **24** 054508
[46] Francisquez M., Bernard T.N., Zhu B., Hakim A., Rogers B.N. and Hammett G.W. 2020 *Phys. Plasmas* **27** 082301
[47] Michels D., Stegmeir A., Ulbl P., Jarema D. and Jenko F. 2021 *Comput. Phys. Commun.* **264** 107986
[48] Dorf M.A., Dorr M.R., Hittinger J.A., Cohen R.H. and Rognlien T.D. 2016 *Phys. Plasmas* **23** 056102
[49] Parisi J.F. *et al* 2022 in preparation
[50] Guttenfelder W., Groebner R., Canik J., Grierson B., Belli E. and Candy J. 2021 *Nucl. Fusion* **61** 056005
[51] Han M., Wang Z.X., Dong J. and Du H. 2017 *Nucl. Fusion* **57** 046019
[52] Pueschel M., Hatch D., Kotschenreuther M., Ishizawa A. and Merlo G. 2020 *Nucl. Fusion* **60** 124005
[53] Morel P., Navarro A.B., Albrecht-Marc M., Carati D., Merz F., Görler T. and Jenko F. 2011 *Phys. Plasmas* **18** 072301
[54] Reshko M. and Roach C.M. 2008 *Plasma Phys. Control. Fusion* **50** 115002